Atmos. Chem. Phys. Discuss., 12, 31107–31151, 2012
www.atmos-chem-phys-discuss.net/12/31107/2012/
doi:10.5194/acpd-12-31107-2012

Atmospheric Chemistry and Physics Discussions

Spatial distribution of dust's optical properties over the Sahara and Asia inferred from Moderate Resolution Imaging Spectroradiometer

M. Yoshida[1,2], **J. M. Haywood**[3], **B. T. Johnson**[3], **H. Murakami**[4], **and T. Nakajima**[1]

[1]Atmosphere and Ocean Research Institute, University of Tokyo, Chiba, Japan
[2]Remote Sensing Technology Center of Japan, Tsukuba, Japan
[3]Met Office Observation Based Research, Exeter, UK
[4]Japan Aerospace Exploration Agency, Tsukuba, Japan

Received: 17 September 2012 – Accepted: 5 November 2012 – Published: 5 December 2012

Correspondence to: M. Yoshida (mayum@restec.or.jp)

Published by Copernicus Publications on behalf of the European Geosciences Union.

Abstract

There is a great deal of uncertainty surrounding the role of mineral dust aerosols in the earth's climate system. One reason for this uncertainty is that the optical properties of mineral dust, such as its single scattering albedo (the ratio of scattering to total extinction), are poorly understood because ground observations are limited to several locations and the satellite standard products are not available due to the excessively bright surface of the desert in the visible wavelength. We develop a method in this paper to estimate the spatial distributions of the aerosol single scattering albedo (ω_0) and optical depth (τ_a), with daily 1 degree latitude and 1 degree longitude resolution, using data from Moderate Resolution Imaging Spectroradiometer (MODIS), as well as model simulations of radiative transfer. This approach is based on the "critical surface reflectance" method developed in the literature, which estimates ω_0 from the top of the atmospheric radiance. We confirm that the uncertainties in our estimation of ω_0 and τ_a are suitably minor and that the characteristic spatial distributions estimated over the Sahara and Asia are significant. The results for the Sahara indicate good correlation between ω_0 and the surface reflectance and between ω_0 and $\tau_{a.}$ Therefore, ω_0 is determined mainly by the mineral composition of surface dust and/or the optical depth of airborne dust in the Sahara. On the other hand, the relationships between ω_0, τ_a, and the surface reflectance are less clear in Asia than in the Sahara, and the values of ω_0 are smaller than those in the Sahara. The regions with small $\omega_0$values are consistent with the regions where coal-burning smoke and carbonaceous aerosols are thought to be transported, as reported in previous studies. Because the coal-burning and carbonaceous aerosols are known to be more absorptive and have smaller ω_0 values than dust aerosols, our results indicate that the dust aerosols in Asia are contaminated by these anthropogenic aerosols. The spatial distribution of dust optical properties obtained in our work could be useful in understanding the roles of dust aerosols in the earth's climate system, most likely through future collaboration with regional and global modelling studies.

ACPD
12, 31107–31151, 2012

1 Introduction

Aerosols are one of the most uncertain factors in determining the energy budget of the earth's climate system. Species of aerosols with significant radiative forcing include sulphates, fossil fuel organics, black carbon, biomass burning, nitrates, and mineral dust (Forster et al., 2007). Among these, mineral dust can both scatter solar radiation to space and absorb solar and terrestrial radiation (e.g. Andreae, 1995). Measurements of mineral dust's direct radiative effect (DRE) over the ocean have suggested that the local DRE could be extremely strong (Forster et al., 2007), and the global DRE of mineral dust based on recent model simulations ranged from −0.56 to +0.1 $\mathrm{W\,m^{-2}}$, indicating major uncertainty on the role of mineral dust in the climate system (Forster et al., 2007).

One reason for this uncertainty regarding the radiative effect of mineral dust is that its optical properties are poorly understood (e.g. Sokolik et al., 2001). Among dust optical parameters, the single scattering albedo (the ratio of scattering to total extinction cross sections) is particularly important for quantifying radiative forcing. For example, Hansen et al. (1997) found that the critical single scattering albedo at which the aerosol's impact on the global mean surface temperature shifted from cooling to heating was approximately 0.91 in the visible spectrum when "semidirect" aerosol effects were included (i.e. the concept that aerosol absorption causes a positive climate feedback by reducing local large-scale cloud cover).

The World Meteorological Organisation (WMO) recommended an imaginary index of refraction of 0.008, corresponding to the dust's single scattering albedo (ω_0) of 0.653 at 0.55 µm (WMO, 1983). However, observations from the ground and in airplanes over the Sahara suggested significantly smaller dust absorption values than the WMO. Haywood et al. (2003) reported values of 0.95–0.99 from the Saharan Dust Experiment (SHADE, Tanré et al., 2003), and McConnell et al. (2008) reported a range of 0.95–0.99 during the Dust Outflow and Deposition to the Ocean experiment (DODO, McConnell et al., 2008). Osborne et al. (2008) estimated the ω_0 for pure dust aerosol

ACPD
12, 31107–31151, 2012

during the Dust and Biomass-burning Experiment (DABEX, Haywood et al., 2008) to be consistently high in the range of 0.98–0.99. According to Johnson and Osborne (2011), ω_0 values of 0.55 µm were measured in the range of 0.92–0.99 during the Geostationary Earth Radiation Budget Intercomparisons of Long-wave and Short-wave Radiation (GERBILS, Haywood et al., 2011) campaign. Analyses of the ω_0 values of Saharan dust from the aerosol robotic network (AERONET, Holben et al., 1998) suggested an average of 0.95 at 0.67 µm (Dubovik et al., 2002).

Ground observations of ω_0 were also performed over the Asian region. Unpolluted Asian dust analysed during the Aeolian Dust Experiment on Climate (ADEC, Mikami et al., 2006) had an average ω_0 of 0.93 at 0.67 µm, and ω_0 values of 0.90 and 0.89 were obtained from ground-based radiation measurements (Kim et al., 2004, 2005). Based on observations at the dust source and surrounding regions, dust over Asia was reported as possibly blackened during movement due to its mixing with soot particles produced over industrial areas (Kim et al., 2004, 2005; Sohn et al., 2007).

The optical properties of dust were obtained from satellite observations in addition to these ground observations. While satellite data can provide continuous observations over large areas, it is not easy to provide aerosol properties over an entire desert area because the desert's surface is too bright in the visible wavelengths. Kaufman et al. (2001) estimated the ω_0 over the Sahara using the "critical surface reflectance" method, which requires information on aerosol optical depth (τ_a), but their analysis was limited to a particular location over the Sahara because they had to use a τ_a value derived from independent ground measurements. The deep blue algorithm (Hsu et al., 2004) retrieved aerosol properties from satellite data over bright surfaces such as arid and semiarid areas, but the researchers estimated ω_0 only at wavelengths below 500 nm and assumed the ω_0 value to be constant at 670 nm. More recently, Zhu et al. (2011) estimated the spatial distribution of absorption by aerosols produced during biomass burning by using the critical surface reflectance method described above, but their method cannot be applied to desert areas because information on τ_a values is not available for such areas.

ACPD
12, 31107–31151, 2012

In summary, the optical properties of dust obtained over desert areas in the literature were generally limited to certain locations due to the difficulty of performing the ground and satellite observations. Therefore, the spatial and temporal distributions of dust's optical properties have not yet been extensively examined. The chemical properties of mineral dust at the earth's surface vary over space and time, and dust aerosols can be mixed with other aerosols during transportation. Therefore, the spatial and temporal distributions of dust's optical properties may affect the climate states over and around a desert area. These distributions have also not been considered in global or regional models (Forster et al., 2007).

In the present study, we investigate the spatial distribution of dust optical properties such as ω_0 and τ_a over desert areas using nine years data of Moderate Resolution Imaging Spectroradiometer (MODIS) on board the Aqua satellite. Special attention is given to the optical properties of dust over the Saharan and Asian desert regions. The general features of the dust aerosol's optical properties are discussed by comparing optical properties between these regions.

Our methodology is based on the theory that the critical surface reflectance, the observed radiance of which is uninfluenced by the variability in dust's optical depth, depends on ω_0 (Kaufman, 1987; Kaufman et al., 2001). Yoshida and Murakami (2008) also used the critical surface reflectance method and investigated the mean value of ω_0 over the Saharan region using long-term MODIS satellite data. We extend the approach of Yoshida and Murakami (2008) and explore the spatial distribution of ω_0 and τ_a at resolutions of 1 degree longitude and 1 degree latitude using daily MODIS data. The details of our methodology are explained in Sect. 2, and Sect. 3 gives the optical properties of dust that we estimated over the Sahara and Asia. Finally, our results are summarised in Sect. 4.

ACPD
12, 31107–31151, 2012

2 Methodology

We estimate the single scattering albedo and optical depth of dust using MODIS satellite data and model simulations based on the method developed by Kaufman (1987) and Kaufman et al. (2001). Basic concept of our methodology is given in Sect. 2.1. Descriptions of the MODIS satellite data and radiative transfer model simulations are given in Sects. 2.2 and 2.3, respectively. Details on the procedure are given in Sect. 2.4 and the interpretation of our formulation with approximated equations is described in Sect. 2.5.

2.1 Basic concept

The basic concept of our methodology is illustrated in Fig. 1. The reflectance at the top of the atmosphere (TOA) is simulated using the radiative transfer model described in Sect. 2.3 under hazy and clear conditions (the definition of hazy and clear conditions is given in Sect. 2.4). Figure 1 shows the difference between the TOA reflectances in hazy and clear conditions ($\Delta\rho^t$) as a function of the TOA reflectance in clear conditions (ρ^t_{clear}) using the radiative transfer model by changing the surface reflectance from 0.1 to 0.5 in the simulation. The single scattering albedo (ω_0) and optical depth (τ_a) of dust are perturbed in Fig. 1. The results for ω_0 = 0.970 (solid), 0.901 (dashed), and τ_a = 1.0 (blue), 2.0 (green), and 3.0 (red) are shown in Fig. 1.

The following is an interpretation of the features in Fig. 1. For dark surfaces (small ρ^t_{clear} in Fig. 1) the TOA reflectance increases as the dust's optical depth increases, whereas for bright surfaces (large ρ^t_{clear} in Fig. 1) the TOA reflectance decreases as the dust's optical depth increases. As shown in Fig. 1, the critical surface reflectance (ρ_c), for which the TOA reflectance (critical TOA reflectance ρ^t_c) is uninfluenced by the variability in the dust's optical depth, depends on ω_0. There is a balance at ρ_c between the brightening of the surface by atmospheric scattering and the darkening of the surface by aerosol absorption (Kaufman, 1987). ρ_c and ρ^t_c can be obtained

ACPD
12, 31107–31151, 2012

by satellite observation; thus, we can estimate ω_0 of the dust based on the radiative transfer model simulation.

In Kaufman (1987) and Kaufman et al. (2001), τ_a values are based on independent ground measurements. In general, the number of ground measurements in the middle of a desert region was very small, and τ_a was not estimated over desert areas in the satellite standard products of the visible wavelengths because the surface albedo of the desert was too high. In this study, τ_a is estimated along with ω_0, making our method more advantageous compared to previous studies because we can estimate τ_a and ω_0 whenever the appropriate satellite data are available, especially over areas where ground measurements are unavailable or desert areas where the satellite standard product are unavailable.

The method we devised in this study is as follows. As illustrated in Fig. 1, the slope of $\rho^t_{\text{clear}} - \Delta\rho^t$ diagram depends on τ_a: the absolute value of a slope is greater for larger τ_a values because if the dust aerosol is thick enough (i.e. τ_a is large), the difference in the TOA reflectance between hazy and clear skies ($\Delta\rho^t$) changes accordingly when we change the surface albedo. We estimate the τ_a and ω_0 values based on the fact that the features of the $\rho^t_{\text{clear}} - \Delta\rho^t$ diagram are dependent on τ_a and ω_0. The $\rho^t_{\text{clear}} - \Delta\rho^t$ diagram is created using the daily 1 degree longitude and 1 degree latitude data from the MODIS satellite, and thus we can estimate τ_a and ω_0 at these space and time resolutions.

2.2 Satellite data

We use Level-1B radiance data sub-sampled at 5 km by the MODIS on board the NASA EOS Aqua spacecraft (http://modis.gsfc.nasa.gov/). The MODIS data for bands 9 (0.438–0.448 µm) and 1 (0.620–0.670 µm) are used for this analysis because these are the bands at which the optical properties of AERONET ground observations are available (Holben et al., 1998). The target area for the analysis is the land area from 10° to 35° north and 20° west to 30° east over the Sahara, and from 34° to 45° north and 75° to 145° east over Asia. We use nine years of data from 2003 to 2011 and select

ACPD
12, 31107–31151, 2012

three-month periods of May–August in the Sahara and March–May in Asia because dust events often occur during these months in each region. To select clear-sky (i.e. cloud-free) conditions, we use the cloud mask from Level2 MODIS atmosphere products (Ackerman et al., 1998). To distinguish between clear and hazy conditions, we use the aerosol index values (Herman et al., 1997; Torres et al., 1998) from the Earth Probe Total Ozone Mapping Spectrometer (TOMS) for 2003–2005 and those from an Ozone Monitoring Instrument (OMI) for 2006–2011 (Torres et al., 2002, 2007).

2.3 Simulations with a radiative transfer model

We use a radiative transfer code called System for the Transfer of Atmospheric Radiation developed at the University of Tokyo (RSTAR, Nakajima and Tanaka, 1986, 1988; Stamnes et al., 1988) for the model simulation. Because many studies indicate that a bimodal lognormal function is the most appropriate model for aerosol particle size distribution (cf. Whitby, 1978; Shettle and Fenn, 1979; Remer and Kaufman, 1998), we use the following dust size (r_d) distribution:

$$\frac{\mathrm{d}V(r_\mathrm{d})}{\mathrm{d}\ln r_\mathrm{d}} = \sum_{i=1}^{2} \frac{C_{\mathrm{v},i}}{\sqrt{2\pi}\ln\sigma_i} \exp\left[-\frac{(\ln r_\mathrm{d} - \ln r_{\mathrm{v},i})^2}{2\ln^2\sigma_i}\right], \quad (1)$$

where the index i denotes the fine ($i = 1$) and coarse ($i = 2$) modes of the aerosol, $C_{\mathrm{v},i}$ is the particle volume concentration, $r_{\mathrm{v},i}$ is the volume median radius, and σ_i is the standard deviation. For the shape of the aerosol, we assume a non-spherical yellow dust model (Nakajima et al., 1989), employing the non-spherical parameters from a semi-empirical theory by Pollack and Cuzzi (1980) with r of 1.1, $X0$ of 7, and G of 10.

The aerosol size distribution parameters ($C_{\mathrm{v},1}$, $r_{\mathrm{v},1}$, σ_1, $C_{\mathrm{v},2}$, $r_{\mathrm{v},2}$, σ_2), and the real part of the refractive index (m_r) in the model simulation are derived from AERONET Level 2.0 inversion data (Dubovik and King, 2000; http://aeronet.gsfc.nasa.gov) for the hazy conditions. The aerosol's optical depth for the clear conditions ($\tau_{\mathrm{a\_clear}}$) is also derived

ACPD
12, 31107–31151, 2012

from AERONET Level 2.0 direct sun algorithm data (O'Neill et al., 2003) in the clear conditions. These values are distinguished as hazy conditions (aerosol index greater than 3) and clear conditions (aerosol index less than or equal to 2) using the simultaneous TOMS or OMI data. Here, we use the TOM and OMI data for the classification of clear and hazy conditions because of the consistency with the classification of MODIS satellite data used for the analysis as described in Sect. 2.4.

The values of model parameters are shown as the "Mean" listed in Table 1. Here, $C_{v,1}$ and $C_{v,2}$ are used for determining the ratio of volume concentration between fine and coarse mode, and the aerosol's total column density is determined by the aerosol's optical depth. In the present study, uncertainties of the model parameters are considered using the "Standard deviation" listed in Table 1. The values of "Mean" and "Standard deviations" in Table 1 are derived from the AERONET data using the observational sites shown in Fig. 4 for the Sahara and Fig. 8 for Asia. The uncertainties in the model simulations concerning the estimation of τ_a and ω_0 are described in Sect. 3.1.

In the radiative transfer simulations, we consider the altitude of the surface over the Sahara and Asia using the ETOPO1 global relief model (Amante and Eakins, 2009). Original ETOPO1 data with 1-min resolution is averaged to 1 degree resolution for the calculation.

2.4 Procedure

This section describes the procedures used for the estimation of τ_a and ω_0. First, we sample the TOA reflectance from the daily MODIS satellite data in clear and hazy conditions with various surface reflectances within 1 degree longitude and 1 degree latitude. Then, we create a scatter plot of the $\rho^t_{clear} - \Delta\rho^t$ diagram and derive the critical TOA reflectance (ρ^t_c) and slope of the diagram (α), as illustrated in Fig. 2. The points in Fig. 2 are obtained from $0.05^\circ \times 0.05^\circ$ MODIS satellite data within the $1^\circ \times 1^\circ$ grid (so the number of points is a maximum of 400). Because the surface reflectance varies spatially, we can obtain the scatter plot shown in Fig. 2 with the daily $1^\circ \times 1^\circ$ resolution.

ACPD
12, 31107–31151, 2012

For clear conditions, we consider the inclusion criterion that the aerosol index obtained from TOMS or OMI on the same day is less than or equal to 2. ρ^t_{clear} is derived from the time average of TOA reflectance during clear conditions. The time average is taken using data for every 16 days (the MODIS recurrence period) due to the surface's bi-directional characteristics and the differences in atmospheric path length and scattering phase function. Therefore, we have 16 different ρ^t_{clear} values according to the MODIS geometry.

For hazy conditions, we consider the criterion that the aerosol index is greater than 3. Here, we choose the $0.05^\circ \times 0.05^\circ$ data with a MODIS cloud mask to be "confidently clear" in the selection of both clear and hazy conditions. For the calculation of $\Delta\rho^t = \rho^t - \rho^t_{\mathrm{clear}}$, we use a ρ^t_{clear} value with geometry identical to that of the ρ^t during hazy conditions.

From the scatter plot of the $\rho^t_{\mathrm{clear}} - \Delta\rho^t$ diagram, we derive the critical surface reflectance (ρ^t_{c}) and slope (α). Both ρ^t_{c} and α are estimated only when they are statistically significant in the least-squares method. The F-statistical test of significance is performed under the assumption that the statistic F described below follows an F-distribution with $(k, n-k-1)$ degrees of freedom:

$$F = \frac{\frac{S_{\mathrm{R}}}{k}}{\frac{S_{\mathrm{E}}}{n-k-1}} = \frac{\frac{R^2}{k}}{\frac{1-R^2}{n-k-1}} \tag{2}$$

where S_{R} is the square sum of the regression, S_{E} is the square sum of errors, R is the multiple correlation coefficient, and n and k are the number of data points and explanatory variables, respectively. We assume the level of significance of rejection to be 5 %.

To connect the values of $[\rho^t_{\mathrm{c}}, \alpha]$ obtained from the scatter plot to the values $[\omega_0, \tau_{\mathrm{a}}]$, we perform the model simulations described in Sect. 2.3 in advance and create the look-up tables (LUTs) as shown in Fig. 3. To calculate the LUTs, we calculate $\Delta\rho^t$ and ρ^t_{clear} by perturbing the surface reflectance and then calculate $[\rho^t_{\mathrm{c}}, \alpha]$ from the $\rho^t_{\mathrm{clear}} -$

ACPD
12, 31107–31151, 2012

$\Delta\rho^t$ diagram. In the calculation of LUTs, we use the two wavelengths corresponding to bands 1 and 9 with various geometries (solar and satellite zenith angles and the azimuth angle between the sun and satellite).

When the surface reflectance is low enough and there are no data with $\Delta\rho^t = 0$ (and thus ρ_c^t), the regression line of the scatter plot is extrapolated to find ρ_c^t where $\Delta\rho^t = 0$. As shown in Fig. 1, the relationship between ρ_{clear}^t and $\Delta\rho^t$ is almost linear, but includes non-linear components. Therefore, we create four different LUTs for the four different surface reflectances (essentially ρ_{clear}^t).

In the present study, the aerosol's optical properties estimated as described above are compared to the ground observations in Sect. 3.2. In the Sahara, the AERONET data (the site locations are indicated in Fig. 4) is used for the validation. In Asia, the observational data from Skyradiometer Network (SKYNET, http://atmos.cr.chiba-u.ac.jp/index.html) are used for the validation (the site locations are shown in Fig. 8).

2.5 Interpretation of the proposed method with approximated equations

To interpret our method for the estimation of dust aerosol's optical properties, we derive the relationship between $[\omega_0, \tau_a]$ and $[\rho_c^t, \alpha]$ with approximated equations that can be obtained under simple conditions. The interpretation of the model simulations using approximated equations for the relationship between ω_0 and ρ_c^t was given in Kaufman (1987), so we focus our attention on the interpretation of τ_a. The relationship between the TOA reflectance (ρ^t) and the reflectance of a Lambert surface (ρ_g) is (Chandrasekhar, 1960):

$$\rho^t = \rho_0^t + T_d T_u \rho_g / (1 - s\rho_g) \quad (3)$$

where ρ_0 is the reflectance of the atmosphere if the ground is non-reflecting ($\rho_g = 0$), T_d is the total transmittance from the top of the atmosphere to the ground, T_u is the total transmittance from the ground to the top of the atmosphere, and s is the fraction of the upward flux reflected back to the surface by the atmosphere. If the solar zenith (θ_0) and

ACPD
12, 31107–31151, 2012

viewing angles (θ) are small enough (Chandrasekhar,1960):

$$\rho_0^t = \pi \sec\theta_0 \sec\theta \omega_0 \frac{p}{4\pi} \tau \tag{4}$$

where p is the scattering phase function, normalised such that its integral over all angles equals 4π. τ is the total optical depth of the gaseous and aerosol scattering. An expression for atmospheric transmission (T_d and T_u) is formulated as (Meador and Weaver 1980):

$$T_d = \exp\left\{\{-\sec\theta_0\}\left\{\tau_a\left[1-\omega_0\left(1-\beta^a\right)\right]+\tau_m/2\right\}\right\} \tag{5}$$

$$T_u = \exp\left\{\{-\sec\theta\}\left\{\tau_a\left[1-\omega_0\left(1-\beta^a\right)\right]+\tau_m/2\right\}\right\} \tag{6}$$

where τ_m is the molecular optical depth, τ_a is the aerosol optical depth, and β^a is the aerosol backscattering fraction (Coakley and Chylek, 1974). By substituting Eqs. (4)–(6) to Eq. (3):

$$\rho^t = \sec\theta_0 \sec\theta \omega_0 \frac{p}{4}\tau + \frac{\rho_g}{\left(1-s\rho_g\right)} \exp\left\{\left\{-\tau_a\left[1-\omega_0\left(1-\beta^a\right)\right]-\tau_m/2\right\}\left\{\sec\theta_0+\sec\theta\right\}\right\} \tag{7}$$

The TOA reflectance during clear conditions can be formulated in the same manner:

$$\rho_{clear}^t = \sec\theta_0 \sec\theta \omega_0 \frac{p}{4}\tau_{clear} + \frac{\rho_g}{\left(1-s\rho_g\right)} \times \exp\left\{\left\{-\tau_{a\_clear}\left[1-\omega_0\left(1-\beta^a\right)\right]-\tau_m/2\right\}\left\{\sec\theta_0+\sec\theta\right\}\right\} \tag{8}$$

where τ_{clear} and τ_{a_clear} are the total and aerosol optical depths during clear conditions, respectively. The relationship between $\Delta\rho^t$ and ρ_{clear}^t is then calculated using Eqs. (7) and (8):

$$\Delta\rho^t = \rho^t - \rho_{clear}^t = \alpha\rho_{clear}^t + \beta \tag{9}$$

ACPD
12, 31107–31151, 2012

α and β in Eq. (9) are calculated as follows:

$$\alpha = \exp\left\{-(\sec\theta_0 + \sec\theta)(\tau_a - \tau_{a\_clear})\left[1 - \omega_0\left(1 - \beta^a\right)\right]\right\} - 1 \quad (10)$$

$$\beta = \sec\theta_0 \sec\theta \omega_0 \frac{p}{4}\left\{\tau - \exp\left\{-(\sec\theta_0 + \sec\theta)(\tau_a - \tau_{a\_clear})\left[1 - \omega_0\left(1 - \beta^a\right)\right]\right\}\tau_{clear}\right\} \quad (11)$$

Here, we assume that the values of ω_0 and β^a are identical in both hazy and clear conditions. In addition, the variation of $s\rho_g$ due to an additional aerosol layer is ignored because the term $s\rho_g$ itself is usually relatively small. α in Eq. (10) is dependent on τ_a, and τ_a increases if the absolute value of α is large.

3 Results and discussion

In this section, uncertainties in our estimation are investigated in Sect. 3.1. Then, we evaluate our method by comparing the dust properties we estimated with ground observations in Sect. 3.2. Results of the spatial distribution of aerosol's optical properties over the Sahara and Asia are presented in Sect. 3.3, and the reasons for the difference in the optical properties between the two regions are discussed in Sect. 3.4.

3.1 Uncertainties in the estimation of dust's optical properties

This section examines the uncertainties in our estimation of dust's ω_0 and τ_a values. There are ten possible reasons for the uncertainties in our method, and they can be classified into two types. One is uncertainties related to the observations (categories (1) to (6) described below), and the other is uncertainties related to the model simulations (categories (7) to (10)). The uncertainty from each component and the total uncertainty over the Sahara and Asia are summarised in Tables 2 and 3, respectively.

ACPD
12, 31107–31151, 2012

3.1.1 Sources of uncertainty

In our method, we assume that the surface reflectance is identical under hazy and clear conditions, and then estimate the daily values of ω_0 and τ_a in $1^\circ \times 1^\circ$ grid points. Therefore, the uncertainties related to the observations come from the following: variations in surface reflectance ((1) variation in the surface reflectance between hazy and clear conditions and (2) bi-directional characteristics of the surface combined with slight variations in the solar zenith angle); spatial variations in aerosol optical characteristics ((3) variation in ω_0 and (4) variation in τ_a) in $1^\circ \times 1^\circ$ grid points; (5) spatial variations in the geometry in $1^\circ \times 1^\circ$ grid points; and (6) satellite calibration errors. The inherent error of the radiative transfer calculation in the model simulations is approximately 0.4 % during hazy and clear conditions if the aerosol model is correct (Nakajima and Tanaka, 1988). Therefore, the uncertainties due to the assumptions of the aerosol model are important. Possible sources of uncertainty include uncertainties in the aerosol model parameters: (7) the optical depth of clear conditions, (8) aerosol size distribution (volume median radius and the ratio of volume concentration between fine and coarse mode), (9) real part of the aerosol refractive index, and (10) dust altitude.

Uncertainties in the surface reflectance, represented by categories (1) and (2), are caused by the variation of the surface reflectance. These variations are evaluated using the MODIS surface reflectance Daily L3 Global 0.05deg CMG data (MYD09CMG). As described in Sect. 2.4, differences in the TOA reflectance between the hazy and clear conditions are derived from 16-day intervals of data based on the satellite geometry. Therefore, we estimate the variation in the surface reflectance between the hazy and clear conditions from the standard deviation of the surface reflectance at each grid point using the clear-sky data at intervals of 16 days. Because the data with wavelengths in band 9 (0.438–0.448 µm) are not available in MYD09CMG, we use the surface reflectance data with the nearest wavelengths (band 3, 0.459–0.479 µm). The standard deviations of the surface reflectance over the Sahara are 0.0077 (band 1) and 0.0083 (band 3) and those over Asia are 0.0131 (band 1) and 0.0135 (band 3).

ACPD
12, 31107–31151, 2012

Uncertainties in the estimation of ω_0 and τ_a are calculated by perturbing the surface reflectance by +/− the standard deviation.

Uncertainties in aerosol optical characteristics, represented by categories (3)–(5), are caused by spatial variation in the optical characteristics. These variations correspond to the spread of the scatter plot in the $\rho^t_{clear} - \Delta\rho^t$ diagram. The uncertainties are caused because ω_0 and τ_a are estimated from the slope α and x-intercept ρ^t_c in the scatter plot by the least-squares method, as shown in Fig. 2. The errors from ρ^t_c and α caused by the least-squares method are shown in (b) and (c) of Tables 2 and 3, respectively.

Category (6), concerning satellite calibration error, results in uncertainty in the TOA reflectance and ρ^t_c values. Assuming the calibration error of the MODIS satellite to be 5 %, the uncertainty in ρ^t_c should also be 5 %. The uncertainty in ω_0 and τ_a due to the satellite calibration is shown in (d) of Tables 2 and 3.

Uncertainties in aerosol model parameters, represented by categories (7)–(9), are calculated by perturbing the aerosol model parameters by the standard deviation, as shown in Table 1. The uncertainties in the model parameters, such as the aerosol's optical depth during clear conditions (τ_{a_clear}), the fine and coarse modes of the volume median radius ($r_{v,1}$, $r_{v,2}$), the fine and coarse modes of the volume concentration ($C_{v,1}$, $C_{v,2}$), and the real part of the refractive index (m_r) are shown in (e), (f), (g), (h), (i), and (j) of Tables 2 and 3, respectively.

Finally, the uncertainties in dust altitude described by category (10) are handled by changing the dust layer in the model simulation. In standard model, we assume that the aerosol layer is at an altitude of 4–8 km. We perform the sensitivity test by changing the dust layer to lower (1–5 km) and higher (7–11 km) altitudes. The uncertainty due to dust altitude is shown in (k) of Tables 2 and 3.

ACPD
12, 31107–31151, 2012

3.1.2 Uncertainty in the estimations

The uncertainty components and total uncertainty over the Sahara and Asia in the estimation of ω_0 and τ_a are shown in Tables 2 and 3, respectively. When estimating ω_0, the largest contribution to the total uncertainty is the variation in surface reflectance, categories (1) and (2), as shown in (a) of Tables 2 and 3. On the other hand, the largest contribution to the total uncertainty in the estimation of τ_a is the spatial variation in aerosol optical characteristics, categories (3)–(5), as shown in (c) of Tables 2 and 3.

We should note that the uncertainty in ω_0 caused by the variation in surface reflectance increases for smaller τ_a values because the uncertainties in ρ_c^t, the x-intercept in the $\rho_{clear}^t - \Delta\rho^t$ diagram, increase with decreasing τ_a, for which the absolute value of the slope (α) decrease. For this reason, we use only MODIS satellite data with $\tau_a > 0.5$ to reduce the uncertainties in this study's estimation of ω_0.

The spatial distribution of the total uncertainties in the estimation of ω_0 and τ_a over the Sahara are shown in Fig. 4. The total uncertainty of ω_0 becomes large over the northwestern region of the Sahara because the dust's optical depth τ_a is not large enough. The total uncertainty of τ_a becomes large over the southern region, which contains AERONET sites, because the uncertainties in the aerosol optical characteristics, categories (3)–(5), are large.

We investigate the spatial and temporal distributions of ω_0 and τ_a over the Sahara and Asia in Sect. 3.3. Compared to these spatial and temporal variances in ω_0 and τ_a (Figs. 7 and. 8), the total uncertainties are concluded to be suitably minor.

3.2 Comparison of dust's optical properties with ground observations

3.2.1 The Sahara

We evaluate our method by comparing the calculated ω_0 and τ_a values with ground observations. We use Level 2.0 inversion data for ω_0 (http://aeronet.gsfc.nasa.gov) and the direct sun algorithm for τ_a (O'Neill et al., 2003) at the AERONET site over

ACPD
12, 31107–31151, 2012

the Sahara (the site locations are indicated in Fig. 4). In Fig. 5, the ω_0 and τ_a values estimated with our method are compared to the AERONET data. The error bars in Fig. 5 represent the total uncertainty calculated at each point described in Sect. 3.1. AERONET data at 440 µm and 675 µm are compared with MODIS bands 9 (0.438–0.448 µm) and 1 (0.620–0.670 µm), respectively.

The ω_0 data from the ground observations are consistent with our estimations, as shown in Fig. 5. The spread in the AERONET data is larger than that in the MODIS data, most likely because the former is in the form of point observations, while the latter is in the form of spatial averages over $1^\circ \times 1^\circ$. On the other hand, the estimated τ_a values are larger than those from the AERONET observations, especially for small τ_a. Although our method tends to overestimate τ_a, our estimations correlate with the AERONET observations (the correlation coefficients are 0.462 and 0.311 at bands 9 and 1, respectively).

In general, when τ_a of the MODIS data are consistent with that of the AERONET observations (points around the $y = x$ line), the error bars of the MODIS data tend to be small, as shown in Fig. 5. On the other hand, when τ_a of the MODIS data are larger than that of the AERONET observations (points well above the $y = x$ line), the error bars tend to be large. Therefore, we calculate the regression line by considering the error bars of τ_a in Fig. 5 as the "measurement error" and giving larger (smaller) weights to the data with smaller (larger) error bars. The regression line that considers measurement error of τ_a (red line in Fig. 5) is more consistent with the AERONET observations.

As discussed in Sect. 3.1, the uncertainties in τ_a are caused by the spread in the $\rho^t_{\text{clear}} - \Delta\rho^t$ diagram, as shown in Table 2c. In general, the data with small slopes α (and small τ_a) tend to be rejected by the statistical test in our method. Therefore, one of the reasons for the overestimation of τ_a in the MODIS data compared to the AERONET observations is that the data with small τ_a are not sampled often in Fig. 5.

ACPD
12, 31107–31151, 2012

3.2.2 Asia

Ground observations are available for the AERONET sites at Dalanzadgrad and Issy-Kul, and for the SKYNET site at Dunhuang, as shown in Fig. 8. However, the observational data synchronised with our MODIS data are available only at Dunhuang (a SKYNET site) on 25 April 2004. We use ω_0 and τ_a from the SKYNET data derived by Hashimoto et al. (2012) for our analysis. Because the radiation bands of the MODIS satellite are not the same as those of SKYNET, we use SKYNET data at 400 µm and 500 µm and interpolate them to determine the value at 0.443 µm for comparison with our data at MODIS band 9 (0.438–0.448 µm, midpoint = 0.443 µm). We also use SKYNET data at 675 µm for comparison with our MODIS band 1 (0.620–0.670 µm) data.

Our estimates of ω_0 from the MODIS satellite data at Dunhuang on 25 April 2004 are 0.93 (band 9) and 0.99 (band 1), while those using the SKYNET data are 0.89 (band 9) and 0.94 (band 1). Our estimates of τ_a at Dunhuang on that day are 1.60 (band 9) and 1.00 (band 1) using MODIS data, while those using SKYNET data are 0.46 (band 9) and 0.45 (band 1). Our calculated results for ω_0 slightly overestimate the SKYNET observations, and those for τ_a are larger than the observation results.

In addition to using the SKYNET observations, we compare our estimates of ω_0 with other observations, although these comparisons are not synchronised. The ω_0 values at 0.5 µm reported at Dunhuang during the years 1998–2000 were 0.89 (Kim et al., 2005) and 0.90 (Kim et al., 2004), and those at Anmyon in the years 1998 and 2000 were 0.86 (Kim et al., 2005) and 0.87 (Kim et al., 2004). Furthermore, the ω_0 at 0.5 µm reported at Anmyon was 0.91 on 7 April 2000 (Sohn et al., 2007). Our estimation of ω_0 around Dunhuang is approximately 0.90–0.95 and that around Anmyon is approximately 0.86–0.93. Therefore, our results of ω_0 are consistent with or slightly larger than those in previous studies.

ACPD
12, 31107–31151, 2012

In conclusion, our estimation of ω_0 is nearly consistent with the ground observations, while τ_a is overestimated in the Asian region. These results are similar to those obtained in the Sahara region.

3.2.3 Effect of overestimating optical depth on the estimation of single scattering albedo

As described in Sects. 3.2.1 and 3.2.2, our estimation of ω_0 is generally consistent with existing observations while that of τ_a is overestimated. This overestimation of τ_a may affect the estimation of ω_0, so we check this relationship in Fig. 6. Because the overestimation of τ_a is generally caused by the overestimation of α, as demonstrated in Fig. 2, we reduce the value of α by two standard deviations and estimate the value of ω_0. As shown in Fig. 6, this reduction of α does not affect the estimation of ω_0 in our method. Therefore, it is reasonable to assume that the overestimation of τ_a does not affect the estimation of ω_0, which is consistent with the ground observations.

3.3 Spatial distribution of aerosol's optical properties over the Sahara and Asia

The spatial distributions of optical properties over the Sahara and Asia are shown in Figs. 7 and 8, respectively. The spatial resolution in these figures is $1^\circ \times 1^\circ$, with the time average taken using daily ω_0 and τ_a values estimated with the 2003–2011 MODIS data.

As shown in Figs. 7 and 8, neither ω_0 nor τ_a are spatially uniform. Compared to the magnitudes of the spatial variations in these figures, the total uncertainties estimated in Sect. 3.1 are suitably small in both the Sahara and Asia. Therefore, we can consider the spatial variations shown in Figs. 7 and 8 to be significant.

To investigate the factors determining the spatial distributions of dust's optical properties, we compare them to the distributions of surface reflectance. We use the bihemispherical reflectance (white-sky albedo) of the MODIS albedo product 16Day L3 data (MCD43C3) and take the time average using the same term as that employed with the MODIS data used to determine ω_0 and τ_a as described in Sect. 2.2. Because data with

ACPD
12, 31107–31151, 2012

wavelengths in band 9 (0.438–0.448 µm) are not available in MCD43C3, we use band 3 data (0.459–0.479 µm), which has the wavelength range closest to that of band 9. Note that we do not use the MODIS products of the surface albedo for the estimation of ω_0 and τ_a, but use the TOA reflectance of clear and hazy conditions (ρ^t_{clear} and $\Delta\rho^t$) in our analysis.

Figure 9 shows the scatter plot of ω_0 and the surface reflectance. ω_0 increases in both the Sahara and Asia when the surface reflectance increases. The correlation coefficients between ω_0 and the surface reflectance are 0.66 and 0.78 for bands 9 and 1, respectively, over the Sahara, and 0.53 and 0.62 for bands 9 and 1, respectively, over Asia. These correlations are both significant, but the correlation of the data for the Sahara is larger than that of the data for Asia. This result is partly because the spread in Asia is larger than that in the Sahara. The upper end of ω_0 in Asia is approximately the same as that in the Sahara, while there are many points with ω_0 values lower than those in the Sahara (Fig. 9).

Previous studies reported ω_0 averages over the Sahara of approximately 0.97–0.99 at 0.5 µm (Haywood et al., 2003; Johnson and Osborne, 2011; McConnell et al., 2008; Osborne et al., 2008) and 0.95 at 0.67 µm (Dubovik et al., 2002), while those over Asia were slightly lower, including 0.89–0.90 at 0.5 µm (at Dunhuang, Kim et al., 2004, 2005), 0.93 at 0.67 µm (unpolluted dust, Mikami et al., 2006), and 0.89 at 0.67 µm (Huang et al., 2009). These results are consistent with our results shown in Fig. 9, in which the average of ω_0 over the Sahara is higher than that over Asia.

One possible reason for the good correlation between ω_0 and the surface reflectance could be that the ω_0 of airborne dust is determined by the mineral composition of the ground surface in arid areas. If the dust on a surface with high reflectivity is transported to the atmosphere, ω_0 should become large.

In addition to the relationships between ω_0 and the surface reflectance, those between ω_0 and τ_a are also shown in Fig. 9. ω_0 decreases for large τ_a values in the Sahara (the correlation coefficients are −0.53 and −0.42 for bands 9 and 1, respectively).

ACPD
12, 31107–31151, 2012

On the other hand, the correlations between ω_0 and τ_a are very small in Asia (−0.10 and 0.05 for bands 9 and 1, respectively).

It is known in the light scattering theory by small particles that ω_0 decreases for larger particle radii at a constant refractive index. The correlation between ω_0 and the particle radius becomes larger at smaller wavelengths. Therefore, one possible reason for the good correlation between ω_0 and τ_a over the Sahara (especially at band 9), although other reasons exist, can be described as follows: the wind is strong and/or there are sufficient dust sources in regions with large dust optical depths. In these regions, large dust particles are often transported to the atmosphere, decreasing the value of ω_0.

3.4 Comparison of dust's optical properties between the Sahara and Asia

Figure 9 shows the good correlation between ω_0 and surface reflectance, as well as between ω_0 and τ_a over the Sahara. Therefore, the ω_0 of airborne dust is determined by the mineral composition of the surface and the optical depth. On the other hand, the correlation coefficient between ω_0 and the surface reflectance is slightly smaller in Asia, and the spread of ω_0 values is large compared to that of the Sahara. In addition, the correlation coefficient between ω_0 and τ_a is insignificant in Asia. Accordingly, there should be additional factors affecting ω_0 in Asia.

To investigate the factors that cause the different features of ω_0 in Asia, we compare the spatial distribution of ω_0 to that of dust emission flux as determined by Mukai et al. (2004). The dust emission flux averaged over 1981–2001 in Mukai et al. (2004) was estimated by a global aerosol transport model (Takemura et al., 2000, 2002a,b). Figure 10 shows the region with large dust emissions in Fig. 4 of Mukai et al. (2004), which can be considered a dust source region and is indicated by red circles. This region is also consistent with the region containing large vertical dust flux estimated in Kang et al. (2011) on 30 March 2007. As shown in Fig. 10, the dust source region in Mukai et al. (2004) is in good agreement with the region identified as having large ω_0 values in our study. This region also corresponds to the Takla Makan and Gobi deserts on geological maps.

ACPD
12, 31107–31151, 2012

In general, dust is transported eastward from the source region in these latitudes (e.g. Huang et al., 2008). We investigate the daily feature of the OMI aerosol index and confirm that the dust clouds formed around the source region are often transported eastward to Eastern China, Korea, or Japan (not shown).

Spatial features of the dust aerosol's ω_0 value as shown in Fig. 10 are consistent with the findings of Kim et al. (2004, 2005), in which the ω_0 values observed around dust source regions such as Dunhuang were large compared to the ω_0 values in areas located farther from the source region, such as Anmyon, Gosan, and Amami-Oshima. Coal-burning smoke mixed with dust was also observed in the regions surrounded by a blue box in Fig. 10 (Herman et al., 1997). Mukai et al. (2004) also estimated that carbonaceous and dust aerosols were transported around the region with the blue box in Fig. 10.

It is well-known that coal-burning smoke and carbonaceous aerosols have relatively large absorptivities compared to dust aerosols (Forster et al., 2007). In our results, the ω_0 values around the blue box in Fig. 10 are small compared to those in the dust source region. Therefore, it is reasonable to assume that the dust transported from the source region is contaminated by coal-burning smoke and/or carbonaceous aerosols around the downstream region indicated by the blue box in Fig. 10. These features are also evident in the scatter plots shown in Fig. 9. In Asia, the spread of the ω_0 scatter plot is large compared to that in the Sahara, and the ω_0 values in Asia are generally smaller than those in the Sahara. The lack of correlation between ω_0 and τ_a also suggests that the ω_0 values in Asia are not strongly influenced by the dust's optical depth or particle radius, although these are important factors determining the ω_0 values in Sahara.

Another possible interpretation of Figs. 9 and 10 is that we sample only the carbonaceous aerosols (or aerosols other than dust) around or east side of the blue box in Fig. 10. In order to test this hypothesis, we count the number of samples of daily data which satisfies the criteria in the analysis (Fig. 11). In the present study, we use the daily data with the TOMS aerosol index (AI) > 3 for the dust conditions in the spring (from March to May) as described in Sect. 2. Figure 11 shows the number of samples

ACPD
12, 31107–31151, 2012

of daily data with the TOMS AI > 3 in the spring and the other seasons, such as the winter (from December to February), summer (from June to August), and autumn (from September to November).

As shown in Fig. 11, the number of samples with TOMS AI > 3 is large in the spring, especially around the Takla Makan Desert and the east side of Gobi Desert. However, the number of samples in the winter, summer, and autumn is very small, except around the Takla Makan Desert in the summer. It is known that the dust storms often occur in the spring (Herman et al., 1997), and Mukai et al. (2004) also reported that the dust aerosol's optical thickness became large during March to May in these regions.

On the other hand, Mukai et al. (2004) suggested that the carbonaceous aerosols are emitted and transported more in the winter (from December to February) compared to other seasons in the eastern part of the Asian region. However, the number of samples with the TOMS AI > 3 is small in the winter compared to that in the spring (Fig. 11). Therefore, it is likely that the majority of the daily data with TOMS AI > 3 in the spring used for the analysis corresponds to the dust aerosols, or the mixture of the dust and other aerosols.

4 Summary

In this study, we develop a method of estimating the optical properties of aerosols, such as single scattering albedo (ω_0) and optical depth (τ_a), with daily $1^\circ \times 1^\circ$ resolution. This approach is based on the critical surface reflectance method developed by Kaufman et al. (1987). By estimating τ_a simultaneously, we can estimate the spatial distributions of ω_0 at inland desert areas for which limited observations are available. We estimate the spatial distributions of ω_0 and τ_a over the Sahara and Asia using nine years of MODIS satellite data of bands 9 (0.438–0.448 µm) and 1 (0.620–0.670 µm).

Our method uses model simulations of radiative transfer to estimate the aerosol's optical properties from the critical surface reflectance obtained with the satellite data. To validate the significance of our results, we also investigate the uncertainties of our

ACPD
12, 31107–31151, 2012

estimation based on possible error sources related to the satellite data and model simulations. We calculate the uncertainties in ω_0 over the Sahara (Asia) to be approximately 0.018 and 0.009 (0.021 and 0.015) for bands 9 and 1, respectively, while the uncertainty in τ_a is approximately 0.226 and 0.221 (0.370 and 0.339) for bands 9 and 1, respectively.

To validate our results, we compare our estimations of ω_0 and τ_a with ground observations and find that ω_0 is consistent with the observations, while τ_a is overestimated. This overestimation is most likely due to the large spread in the estimated τ_a values, and small τ_a values tend to be rejected by the significance test. However, we confirm that the overestimation of τ_a does not affect the results for ω_0.

We find significant spatial distributions of ω_0 and τ_a over the Sahara and Asia, as shown in Figs. 7 and 8. To interpret the features of these spatial distributions, we investigate the relationship between ω_0, τ_a, and the surface reflectance (Fig. 9) and observe good correlation between ω_0 and the surface reflectance in both the Sahara (0.66 and 0.78 for bands 9 and 1, respectively) and Asia (0.53 and 0.62 for bands 9 and 1, respectively). The spread of ω_0 is larger and the value of ω_0 is smaller in Asia than in the Sahara when the surface reflectance is kept constant (Fig. 9). In addition, the correlation between ω_0 and τ_a is significant in the Sahara (with correlation coefficients of -0.53 and -0.42 for bands 9 and 1, respectively), but very small in Asia (-0.10 and 0.05 for bands 9 and 1, respectively).

Because there is good correlation between ω_0 and the surface reflectance and between ω_0 and τ_a in the Sahara, ω_0 is determined mainly from the mineral composition of the surface and optical depth of the airborne dust. In regions with large optical depths, the large dust particles are possibly transported to the atmosphere due to the strong wind and/or sufficient dust sources, decreasing the value of ω_0. Therefore, it is reasonable to assume that the ω_0 of airborne dust over the Sahara is essentially controlled by natural factors.

On the other hand, the relationships between ω_0, τ_a, and the surface reflectance in Asia are less clear than those in the Sahara and the ω_0 values are generally smaller

ACPD
12, 31107–31151, 2012

than those in the Sahara (Fig. 9). In terms of the spatial distribution of ω_0, the regions with high ω_0 values agrees well with the Takla Makan and Gobi Desert regions as well as the source region of dust aerosols estimated by a global aerosol transport model in Mukai et al. (2004), as shown by red circles in Fig. 10. In addition, the ω_0 values are small around the regions in which coal-burning smoke was observed (Herman et al., 1997) and the carbonaceous aerosols were transported in a global model (Mukai et al., 2004), as shown by blue box in Fig. 10. Considering that anthropogenic aerosols have relatively large absorptivity and therefore smaller ω_0 values compared to dust aerosols (Forster et al., 2007), our results indicate that dust aerosols are contaminated by these anthropogenic aerosols in adjacent regions.

Our analysis reveals distinct differences in the spatial distributions of dust properties between the Saharan and Asian regions. Our results concerning dust's optical properties may be useful in understanding the roles of dust aerosols in the earth's climate system, as discussed in Sect. 1. The spatial distributions of dust in the Sahara may contain information on the dynamic behaviour of dust aerosols, and the relationships between ω_0 and the surface reflectance and between ω_0 and τ_a could be especially useful for the validation of dust transport processes in numerical models. The spatial distribution of ω_0 we estimated over Asia could also be helpful in understanding the mixing processes of dust and anthropogenic aerosols, such as smoke and carbonaceous aerosols. Finally, our method allows the optical properties of aerosols to be estimated on a daily basis with spatial distributions of $1^\circ \times 1^\circ$ when the satellite data with appropriate conditions are available. If the quality and quantity of satellite data are improved in the future, analyses using the method proposed in this paper will contribute to advance knowledge on the uncertainties of aerosol's optical properties.

Acknowledgements. The authors are grateful to the Open CLASTER project for allowing us to use the RSTAR package for this research. We would like to thank the AERONET project and its staff for establishing and maintaining the Tamanrasset, Agoufou, Banizoumbou and Saada sites considered in this investigation. We would also like to thank the SKYNET project and its staff for establishing and maintaining the Dunhuang site. Finally, we appreciate the valuable discussions

ACPD
12, 31107–31151, 2012

and support provided by Satoru Fukuda, Yosuke Sato, Eiji Oikawa, Makiko Hashimoto, Yasushi Mitomi and Matthew Collins.

References

Ackerman, S. A., Strabala, K. I., Menzel, W. P., Frey, R. A., Moeller, C. C., and Gumley, L. E.: Discriminating clear sky from clouds with MODIS, J. Geophys. Res., 103, 32141–32157, 1998.

Amante, C. and Eakins, B. W.: ETOPO1 1 Arc-Minute Global Relief Model: Procedures, Data Sources and Analysis, NOAA Technical Memorandum NESDIS NGDC-24, 19 pp., NOAA-National Geophysical Data Center, Colorado USA, March 2009.

Andreae, M. O.: World survey of climatology, in: Future Climates of the World, edited by: Henderson-Sellers, A., Elsevier, Amsterdam, Vol. 16, 1995.

Chandrasekhar, S.: Radiative Transfer, Dover, New York, 1960.

Coakley, J. A. and Chylek, P.: The two stream approximation in radiative transfer including the angle of incident radiation, J. Atmos. Sci., 32, 409–418, 1974.

Dubovik, O. and King, M. D.: A flexible inversion algorithm for retrieval of aerosol optical properties from Sun and sky radiance measurements, J. Geophys. Res., 105, 20673–20696, 2000.

Dubovik, O., Holben, B. N., Eck, T. F., Smirnov, A., Kaufman, Y. J., King, M. D., Tanré, D., and Slutsker, I.: Variability of absorption and optical properties of key aerosol types observed in worldwide locations, J. Atmos. Sci, 59, 590–608, 2002.

Forster, P., Ramaswamy, V., Artaxo, P., Berntsen, T., Betts, R., Fahey, D. W., Haywood, J., Lean, J., Lowe, D. C., Myhre, G., Nganga, J., Prinn, R., Raga, G., Schulz, M., and Van Dorland, R.: Changes in atmospheric constituents and in radiative forcing, in: Climate Change 2007: The Physical Science Basis, Contribution of Working Group I to the Fourth Assessment Report of the Intergovernmental Panel on Climate Change, edited by: Solomon, S., Qin, D., Chen, Z., Manning, M., Marquis, M., Averyt, K. B., Tignor, M., and Miller, H. L., Cambridge University Press, Cambridge, UK and New York, NY, USA, 129–234, 2007.

Hansen, J., Sato, M., and Ruedy, R.: Radiative forcing and climate response, J. Geophys. Res., 102, 6831–6864, 1997.

ACPD

12, 31107–31151, 2012

Hashimoto, M., Nakajima, T., Dubovik, O., Campanelli, M., Che, H., Khatri, P., Takamura, T., and Pandithurai, G.: Development of a new data-processing method for SKYNET sky radiometer observations, Atmos. Meas. Tech. Discuss., 5, 4361–4407, doi:10.5194/amtd-5-4361-2012, 2012.

Haywood, J. M., Francis, P., Osborne, S., Glew, M., Loeb, N., Highwood, E., Tanre, D., Myhre, G., Formenti, P., and Hirst, E.: Radiative properties and direct radiative effect of Saharan dust measured by the C-130 aircraft during SHADE: 1. Solar spectrum, J. Geophys. Res., 108, 8577, doi:10.1029/2002JD002687, 2003.

Haywood, J. M., Pelon, J., Formenti, P., Bharmal, N., Brooks, M., Capes, G., Chazette, P., Chou, C., Christopher, S., Coe, H., Cuesta, J., Dermian, Y., Desboeufs, K., Greed, G., Harrison, M. A. J., Heese, B., Highwood, E. J., Johnson, B. T., Mallet, M., Marticorena, B., Marsham, J., Milton, S. F., Myhre, G., Osborne, S. R., Parker, D. J., Rajot, J.-L., Schulz, M., Slingo, A., Tanré, D., and Tulet, P.: Overview of the dust and biomassburning experiment and african multidisciplinary monsoon analysis special observing period-0, J. Geophys. Res., 113, D00C17, doi:10.1029/2008JD010077, 2008.

Haywood, J. M., Johnson, B. T., Osborne, S. R., Baran, A. J., Brooks, M., Milton, S. F., Mulcahy, J, Walters, D., Allan, R. P., Klaver, A., Formenti, P., Brindley, H. E., Christopher, S., and Gupta, P.: Motivation, rationale and key results from the GERBILS Saharan dust measurement campaign, Q. J. Roy. Meteorol. Soc., 137, 1106–1116. doi:10.1002/qj.797, 2011.

Herman, J. R., Bhartia, P. K., Torres, O., Hsu, C., Seftor, C., and Celarier, E., Global distribution of UV-absorbing aerosols from Nimbus 7/TOMS data, J. Geophys. Res., 102, 16911–16922, 1997.

Holben, B. N., Eck, T. F., Slutsker, I., Tanr'e, D., Buis, J. P., Setzer, A., Vermote, E., Reagan, J. A., Kaufman, Y., Nakajima, T., Lavenu, F., Jankowiak, I., and Smirnov, A.: A federated instrument network and data archive for aerosol characterization, Remote Sens. Environ., 66, 1–16, 1998.

Hsu, N. C., Tsay, S.-C., King, M. D., and Herman, J. R.: Aerosol properties over bright-reflecting source regions, IEEE T. Geosci. Remote Sensing, 42, 557–569, 2004.

Huang, J., Minnis, P., Chen, B., Huang, Z., Liu, Z., Zhao, Q., Yi, Y., and Ayers, J. K.: Long-range transport and vertical structure of Asian dust from CALIPSO and surface measurements during PACDEX, J. Geophys. Res., 113, D23212, doi:10.1029/2008JD010620, 2008.

Huang, J., Fu, Q., Su, J., Tang, Q., Minnis, P., Hu, Y., Yi, Y., and Zhao, Q.: Taklimakan dust aerosol radiative heating derived from CALIPSO observations using the Fu-Liou radiation

ACPD
12, 31107–31151, 2012

model with CERES constraints, Atmos. Chem. Phys., 9, 4011–4021, doi:10.5194/acp-9-4011-2009, 2009.
Johnson, B. T. and Osborne, S. R.: Physical and optical properties of mineral dust aerosol measured by aircraft during the GERBILS campaign, Q. J. Roy. Meteorol. Soc., 137, 1117–1130. doi:10.1002/qj.777, 2011.
Kang, J.-Y., Yoon, S.-C., Shao, Y., and Kim, S.-W.: Comparison of vertical dust flux by implementing three dust emission schemes in WRF/Chem, J. Geophys. Res., 116, D09202, doi:10.1029/2010JD014649, 2011.
Kaufman, Y. J.: Satellite sensing of aerosol absorption, J. Geophys. Res., 92, 4307–4317, 1987.
Kaufman, Y. J., Tanré, D., Dubovik, O., Karnieli, A., and Remer, L. A.: Absorption of sunlight by dust as inferred from satellite and ground-based remote sensing, Geophys. Res. Lett., 28, 1479–1482, 2001.
Kim, D.-H., Sohn, B.-J., Nakajima, T., Takamura, T., Takemura, T., Choi, B.-C., and Yoon, S.-C.: Aerosol optical properties over East Asia determined from ground-based sky radiation measurement, J. Geophys. Res., 109, D02209, doi:10.1029/2003JD003387, 2004.
Kim, D.-H., Sohn, B.-J., Nakajima, T., and Takamura, T.: Aerosol radiative forcing over East Asia determined from ground-based solar radiation measurements, J. Geophys. Res., 110, D10S22, doi:10.1029/2004JD004678, 2005.
McConnell C. L., Highwood E. J., Coe H., Formenti P., Anderson B., Osborne S. R., Nava S., Desboeufs K., Chen G., and Harrison M. A. J.: Seasonal variations of the physical and optical characteristics of Saharan dust: results from the Dust Outflow and Deposition to the Ocean (DODO) experiment, J. Geophys. Res., 113, D14S05, doi:10.1029/2007JD009606, 2008.
Meador, W. E. and Weaver, W. R.: Two-stream approximations to radiative transfer in planetary atmospheres: a unified description of existing methods and a new improvement, J. Atmos. Sci., 37, 630–643, 1980.
Mikami, M., Shi, G. Y., Uno, I., Yabuki, S., Iwasaka, Y., Yasui, M., Aoki, T., Tanaka, T. Y., Kurosaki, Y., Masuda, K., Uchiyama, A., Matsuki, A., Sakai, T., Takemi, T., Nakawo, M., Seino, N., Ishizuka, M., Satake, S., Fujita, K., Hara, Y., Kai, K., Kanayama, S., Hayashi, M., Du, M., Kanai, Y., Yamada, Y., Zhang, X. Y., Shen, Z., Zhou, H., Abe, O., Nagai, T., Tsutsumi, Y., Chiba, M., and Suzuki, J.: Aeolian dust experiment on climate impact: an overview of Japan-China Joint Project ADEC, Global Planet. Change, 52, 142–172, doi:10.1016/j.gloplacha.2006.03.001, 2006.

ACPD
12, 31107–31151, 2012

Mukai, M., Nakajima, T., and Takemura, T.: A study of long-term trends in mineral dust aerosol distributions in Asia using a general circulation model, J. Geophys. Res., 109, D19204, doi:10.1029/2003JD004270, 2004.
Nakajima, T. and Tanaka, M.: Matrix formulation for the transfer of solar radiation in a plane-parallel scattering atmosphere, J. Quant. Spectrosc. Ra., 35, 13–21, 1986.
Nakajima, T. and Tanaka, M.: Algorithms for radiative intensity calculations in moderately thick atmospheres using a truncation approximation, J. Quant. Spectrosc. Ra., 40, 51–69, 1988.
Nakajima, T., Tanaka, M., Yamano, M., Shiobara, M., Arao, K., and Nakanishi, Y.: Aerosol optical characteristics in the yellow sand events observed in May, 1982 in Nagasaki – Part II Model, J. Meteorol. Soc. Jpn., 67, 279–291, 1989.
O'Neill, N. T., Eck, T. F., Smirnov, A., Holben, B. N., and Thulasiraman, S.: Spectral discrimination of coarse and fine mode optical depth, J. Geophys. Res., 108, 4559–4573, doi:10.1029/2002JD002975, 2003.
Osborne, S. R., Johnson, B. T., Haywood, J. M., Baran, A. J., Harrison, M. A. J., and McConnell, C. L.: Physical and optical properties of mineral dust aerosol during the dust and biomass-burning experiment, J. Geophys. Res., 113, D00C03, doi:10.1029/2007JD009551, 2008.
Pollack, J. B. and Cuzzi, J. N.: Scattering by non-spherical particles of size comparable to a wavelength: A new semi-empirical theory and its application to tropospheric aerosols, J. Atmos. Sci., 37, 868–881, 1980.
Remer, L. A. and Kaufman, Y. J.: Dynamic aerosol model: urban/industrial aerosol, J. Geophys. Res., 103, 13859–13871, 1998.
Shettle, E. P. and Fenn, R. W.: Models for the aerosol lower atmosphere and the effects of humidity variations on their optical properties, Rep. Tr-79-0214, US Air Force Geophysics Laboratory, Hanscom Air Force Base, Massachusetts, 1979.
Sohn, B.-J., Nakajima, T., Chun, H.-W., and Aoki, K.: More absorbing dust aerosol inferred from sky radiometer measurements at Anmyeon, Korea, J. Meteorol. Soc. Jpn., 85, 815–823, 2007.
Sokolik, I. N., Winker, D. M., Bergametti, G., Gillette, D. A., Carmichael, G., Kaufman, Y. J., Gomes, L., Schuetz, L., and Penner, J. E.: Introduction to special section: outstanding problems in quantifying the radiative impacts of mineral dust, J. Geophys. Res., 106, 18015–18027, 2001.

ACPD
12, 31107–31151, 2012

Stamnes, K., Tsay, S. C., Wiscombe, W., and Jayaweera, K.: Numerically stable algorithm for discrete-ordinate-method radiative transfer in multiple scattering and emitting layered media, Appl. Optics, 27, 2502–2509, 1988.

Takemura, T., Okamoto, H., Maruyama, Y., Numaguti, A. Higurashi, A., and Nakajima, T.: Global three-dimensional simulation of aerosol optical depth distribution of various origins, J. Geophys. Res., 105, 17853–17873, 2000.

Takemura, T., Nakajima, T., Dubovik, O., Holben, B. N., and Kinne, S.: Single scattering albedo and radiative forcing of various aerosol species with a global three-dimensional model, J. Climate, 15, 333–352, 2002a.

Takemura, T., Uno, I., Nakajima, T., Higurashi, A., and Sano, I.: Modeling study of long-range transport of Asian dust and anthropogenic aerosols from East Asia, Geophys. Res. Lett., 29, 2158, doi:10.1029/2002GL016251, 2002b.

Tanré, D., Haywood, J., Pelon, J., Léon, J. F., Chatenet, B., Formenti, P., Francis, P., Goloub, P., Highwood, E. J., and Myhre, G.: Measurement and modeling of the Saharan dust radiative impact: overview of the Saharan Dust Experiment (SHADE), J. Geophys. Res., 108, 8574, doi:10.1029/2002JD003273, 2003.

Torres, O., Bhartia, P. K., Herman, J. R., Ahmad, Z., and Gleason, J.: Derivation of aerosol properties from satellite measurements of backscattered ultraviolet radiation, theoretical basis, J. Geophys. Res.,103, 17099–17110, 1998.

Torres, O., Bhartia, P. K., Herman, J. R., Sinyuk, A., Ginoux, P., and Holben, B.: A long term record of aerosol optical depth from TOMS observations and comparison to AERONET measurements, J. Atmos. Sci., 59, 398–413, 2002.

Torres, O., Tanskanen, A., Veihelman, B., Ahn, C., Braak, R., Bhartia, P. K., Veefkind, P., and Levelt, P.: Aerosols and surface UV products from OMI observations: an overview, J. Geophys. Res., 112, D24S47, doi:10.1029/2007JD008809, 2007.

Whitby, K. T.: The physical characteristics of sulfur aerosols, Atmos. Environ., 12, 135–159, 1978.

World Meteorological Organization: WMO Report of the Experts Meeting on Aerosols and their Climatic Effects, Rep. WCP-55, World Climate Program, Geneva, 1983.

Yoshida, M. and Murakami, H.: Dust absorption averaged over the Sahara inferred from moderate resolution imaging spectroradiometer data, Appl. Opics., 47, 1995–2003, 2008.

ACPD
12, 31107–31151, 2012

Zhu, L., Martins, J. V., and Remer, L. A.: Biomass burning aerosol absorption measurements with MODIS using the critical reflectance method, J. Geophys. Res., 116, D07202, doi:10.1029/2010JD015187, 2011.

ACPD
12, 31107–31151, 2012

Table 1. Mean values and standard deviations of the aerosol model parameters calculated from AERONET data.

Model parameters		Sahara		Asia	
		Mean	Standard deviation	Mean	Standard deviation
Volume median radius (μm)	Fine mode ($r_{v,1}$)	0.183	0.040	0.155	0.034
	Coarse mode ($r_{v,1}$)	2.127	0.309	2.355	0.450
Standard deviation	Fine mode (σ_1)	1.865	–	1.751	–
	Coarse mode (σ_2)	1.785	–	1.845	–
Particle volume concentration ($\mu m^3\,\mu m^{-2}$)	Fine mode ($C_{v,1}$)	0.026	0.011	0.062	0.055
	Coarse mode ($C_{v,2}$)	0.385	0.240	0.486	0.431
Real part of the refractive index	Band 9 (m_r)	1.497	0.045	1.523	0.062
	Band 1 (m_r)	1.508	0.038	1.534	0.051
Aerosol optical depth for clear conditions	Band 9 (τ_{a_clear})	0.254	0.114	0.241	0.126
	Band 1 (τ_{a_clear})	0.212	0.116	0.196	0.134

ACPD
12, 31107–31151, 2012

Table 2. Uncertainties in ω_0 and τ_a due to error sources, shown from (1) to (10) for bands 9 and 1 over the Sahara. The total uncertainties are shown in the rightmost column. The uncertainties related to the observations are (1)–(2) variation in surface reflectance; (3)–(5) spatial variation in aerosol optical characteristics and geometry; and (6) satellite calibration error. The uncertainties related to the model simulations are those in model parameters (7), (8), (9), and (10). Details on each factor are described in the main text.

Optical properties	Error sources											
	Satellite data				Model parameters							Total
	(a) Surface reflectance (1)(2)	(b) ρ_c^t (3)–(5)	(c) α (3)–(5)	(d) Satellite Calibration (6)	(e) $\tau_{a,clear}$ (7)	(f) $r_{v,1}$ (8)	(g) $r_{v,2}$ (8)	(h) $C_{v,1}$ (8)	(i) $C_{v,2}$ (8)	(j) m_r (9)	(k) Altitude (10)	(l) Total
ω_0 (band 9)	0.011	0.001	0.001	0.007	0.002	0.002	0.002	0.002	0.004	0.008	0.009	0.018
ω_0 (band 1)	0.007	0.001	0.002	0.003	0.002	0.001	0.002	0.001	0.001	0.003	0.002	0.009
τ_a (band 9)	0.048	0.014	0.148	0.053	0.099	0.039	0.025	0.036	0.048	0.061	0.065	0.226
τ_a (band 1)	0.056	0.022	0.152	0.054	0.080	0.037	0.042	0.041	0.054	0.060	0.036	0.221

ACPD
12, 31107–31151, 2012

Table 3. Same as Table 2, but for Asia.

Optical properties	Error sources											
	Satellite data				Model parameters							Total
	(a) Surface reflectance (1)(2)	(b) ρ_c^t (3)–(5)	(c) α (3)–(5)	(d) Satellite Calibration (6)	(e) $\tau_{a,clear}$ (7)	(f) $r_{v,1}$ (8)	(g) $r_{v,2}$ (8)	(h) $C_{v,1}$ (8)	(i) $C_{v,2}$ (8)	(j) m_r (9)	(k) Altitude (10)	(l) Total
ω_0 (band 9)	0.011	0.001	0.001	0.007	0.001	0.004	0.001	0.007	0.004	0.006	0.011	0.021
ω_0 (band 1)	0.010	0.002	0.003	0.005	0.002	0.003	0.002	0.005	0.005	0.003	0.002	0.015
τ_a (band 9)	0.046	0.015	0.310	0.057	0.011	0.059	0.011	0.105	0.091	0.080	0.077	0.370
τ_a (band 1)	0.056	0.020	0.258	0.057	0.028	0.058	0.028	0.115	0.136	0.067	0.019	0.339

ACPD
12, 31107–31151, 2012

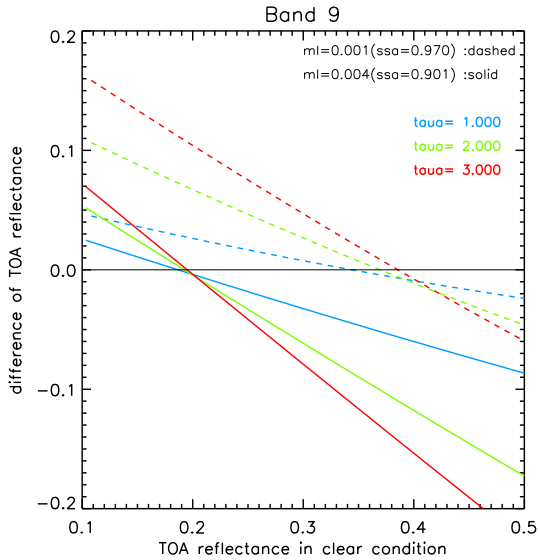

Fig. 1. A sample radiative transfer model simulation to illustrate the essence of the "critical surface reflectance" method developed by Kaufman (1987). The horizontal axis is the top-of-the-atmosphere (TOA) reflectance in clear conditions and the vertical axis is the difference in TOA reflectance between hazy and clear conditions. The lines in the diagram are calculated by changing the surface reflectance from 0.0 to 0.6 (intervals of 0.01) in the model simulations. The dust optical parameters, such as the single scattering albedo (ω_0) and optical depth (τ_a), are perturbed in the model simulations. The dashed line represents the simulation with ω_0 =0.970 (ω_0 is perturbed through the imaginary refractive index, r_i, and in this case r_i = 0.001), and the solid line is that with ω_0 = 0.901 (r_i = 0.004). The optical depths of the dust aerosols used in the simulations are 1.0 (blue), 2.0 (green), and 3.0 (red). The simulations are performed at a solar zenith angle of 10°, satellite zenith angle of 30°, and relative azimuth angle of 180°, and the wavelength is 0.443 µm. The model parameters related to the dust aerosols are given by the "Mean" values in Table 1.

ACPD
12, 31107–31151, 2012

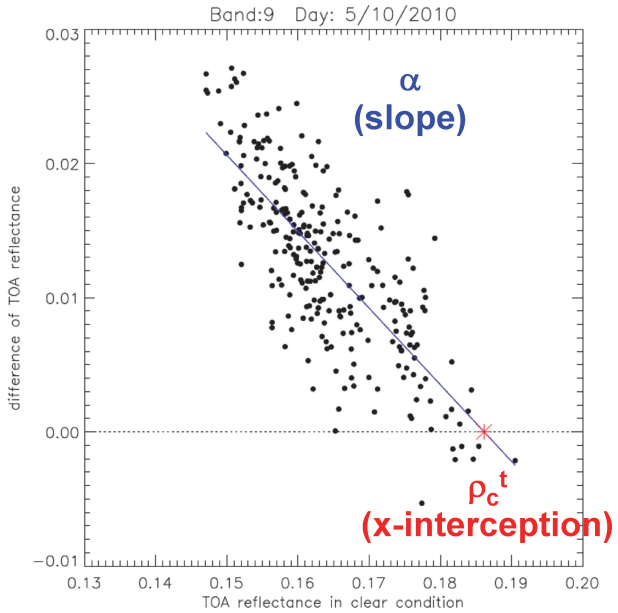

Fig. 2. This figure is identical to Fig. 1, but created from the MODIS satellite data. Each dot is calculated from TOA reflectances with 0.05 degree and 0.05 degree data on 10 May 2010. The mean observed geometry is a solar zenith angle of 17.1°, satellite zenith angle of 42.4°, and relative azimuth angle of 159.8°, and the wavelength is 0.443 µm. This diagram is created using daily TOA reflectance data within a 1 degree and 1 degree grid box, and thus the maximum number of points in a diagram is 400. The fitted line (blue) is calculated with the least-squares method, after which the x-interception (critical surface reflectance ρ_c^t) and slope (α) are estimated. From the look-up table for the relationship between [ρ_c^t, α] and [single scattering albedo (ω_0), optical depth (τ_a)] as shown in Fig. 3, the ω_0 and τ_a values are estimated from the daily 1 degree and 1 degree resolution.

ACPD
12, 31107–31151, 2012

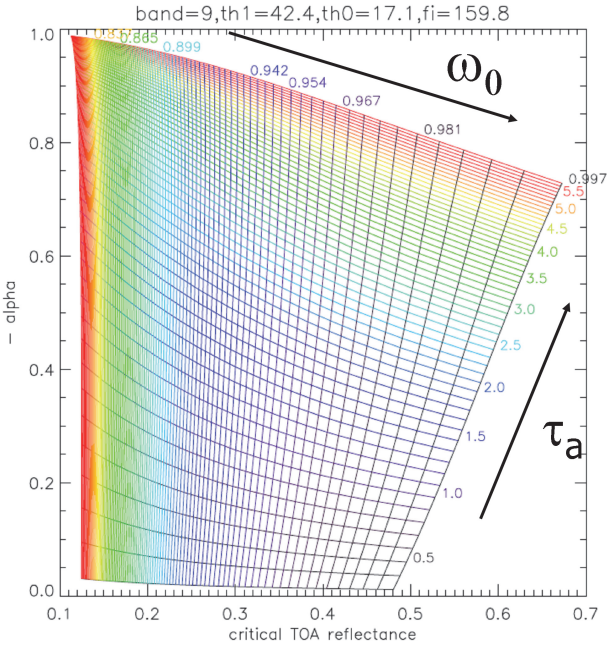

Fig. 3. An example of a look-up table (LUT) calculated from the radiative transfer model simulations. The LUT is used to estimate the dust's single scattering albedo (ω_0) and optical depth (τ_a) from the values of the x-interception (critical surface reflectance ρ_c^t) and the slope (α) as defined in Fig. 2. Here, we give 100 different ω_0 values (through perturbing the imaginary part of the refractive index) and 57 different τ_a values in the model simulation, and then calculate the ρ_c^t and α values as demonstrated in Fig. 1. The satellite and solar geometry, aerosol model parameters, and wavelength are the same as those in Fig. 2.

ACPD
12, 31107–31151, 2012

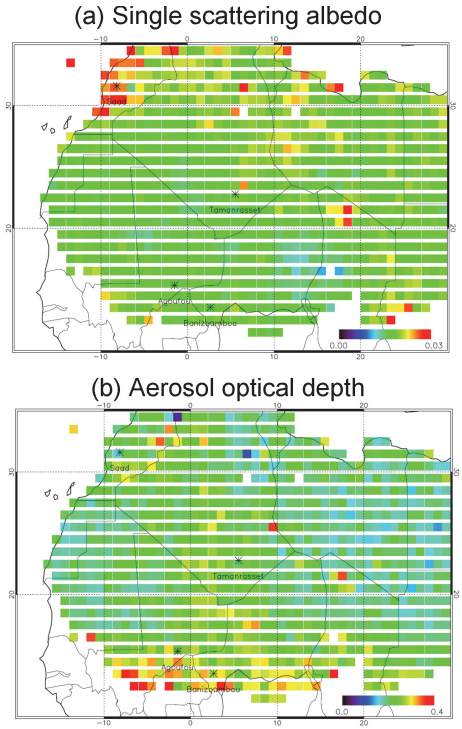

Fig. 4. Spatial distribution of the total uncertainties in band 9 for the estimation of the **(a)** single scattering albedo ω_0 and **(b)** optical depth τ_a over the Sahara. The AERONET sites of Agoufou, Banizoumbou, Saad, and Tamanrasset are also shown.

ACPD
12, 31107–31151, 2012

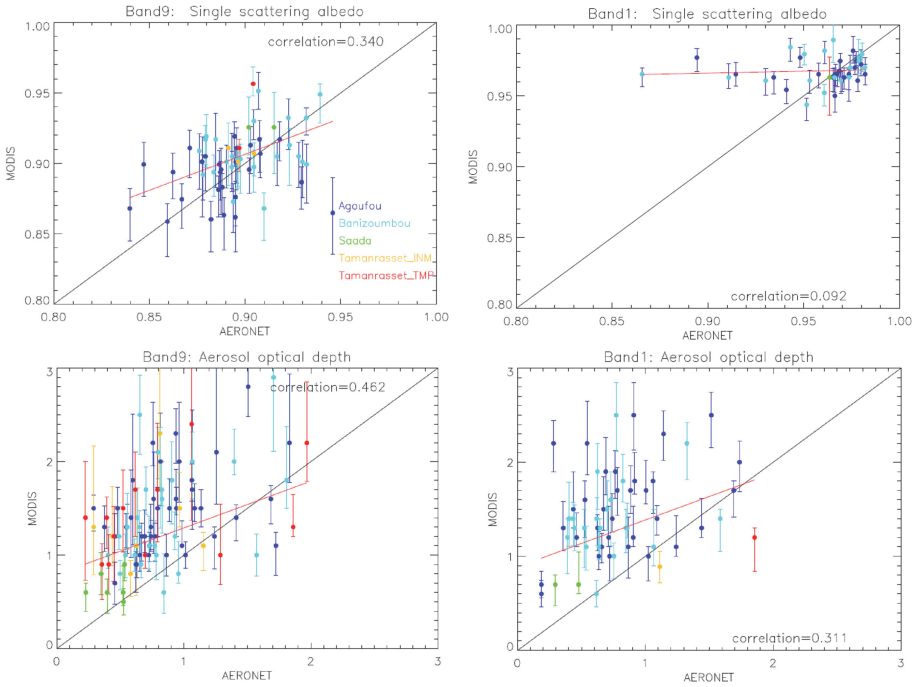

Fig. 5. Comparison of the single scattering albedo (ω_0) and optical depth (τ_a) values we estimated from the MODIS satellite data and model simulations with the AERONET ground observational data. The error bars are the total uncertainty described in Sect. 3.1. We sample the results of grid boxes that include the AERONET sites Agoufou (blue), Banizoumbou (light blue), Saada (green), Tamanrasset_INM (orange), and Tamanrasset_TMP (red). The red line indicates the regression by considering the error bars as the "measurement error", the details of which are described in the main text.

ACPD
12, 31107–31151, 2012

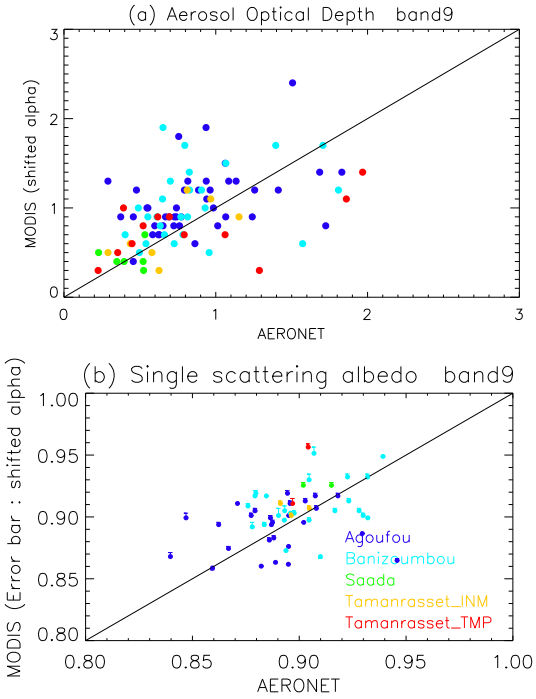

Fig. 6. The effect of overestimating the aerosol optical depth (τ_a) on the estimation of the single scattering albedo (ω_0) in band 9. The horizontal axis represents the observed aerosol optical properties at the AERONET sites (the colours are the same as those in Fig. 5). **(a)** τ_a calculated by reducing the slope α in Fig. 2 by two standard deviations and **(b)** the same ω_0 as in Fig. 5, but the error bars represent the difference between the value in Fig. 5 and the ω_0 value estimated by reducing α by two standard deviations. The standard deviations are estimated from the uncertainty in α as described in Sect. 3.1.

ACPD
12, 31107–31151, 2012

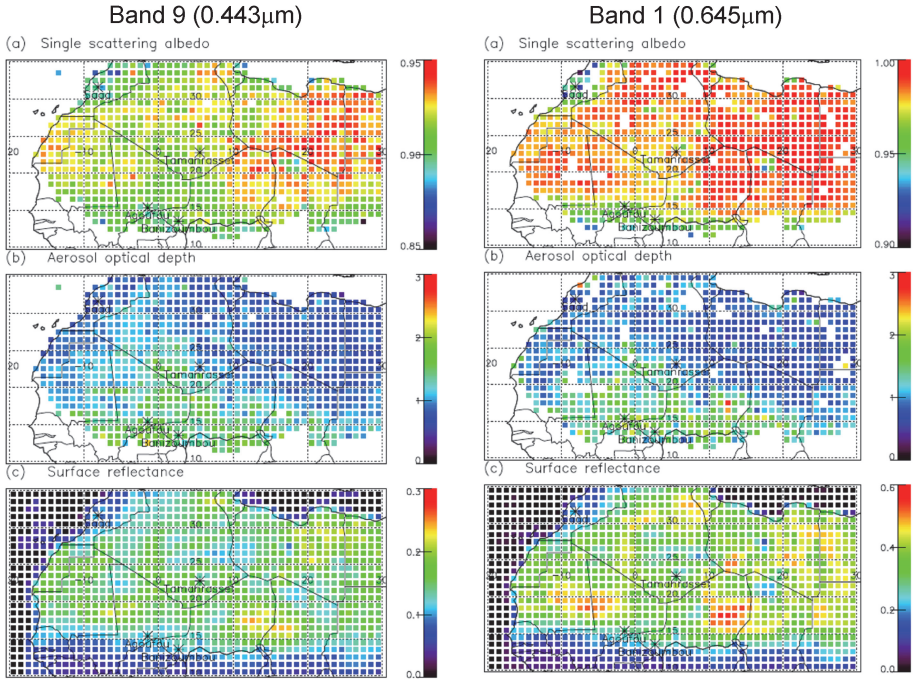

Fig. 7. The spatial distribution of **(a)** single scattering albedo ω_0, **(b)** aerosol optical depth τ_a, and **(c)** surface reflectance in the Sahara. **(a)** and **(b)** are estimated by our method using the 9-yr (2003–2012) May–August data from MODIS and model simulations. **(c)** is obtained from the MODIS albedo 16Day L3 data product (MCD43C3, bihemispherical reflectance). The spatial resolution is 1 degree and 1 degree and the results are based on the time average. The number of MODIS data points in the white grid boxes that satisfy the conditions described in Sect. 2 is less than two. The AERONET sites of Agoufou, Banizoumbou, Saad, and Tamanrasset are also shown.

ACPD
12, 31107–31151, 2012

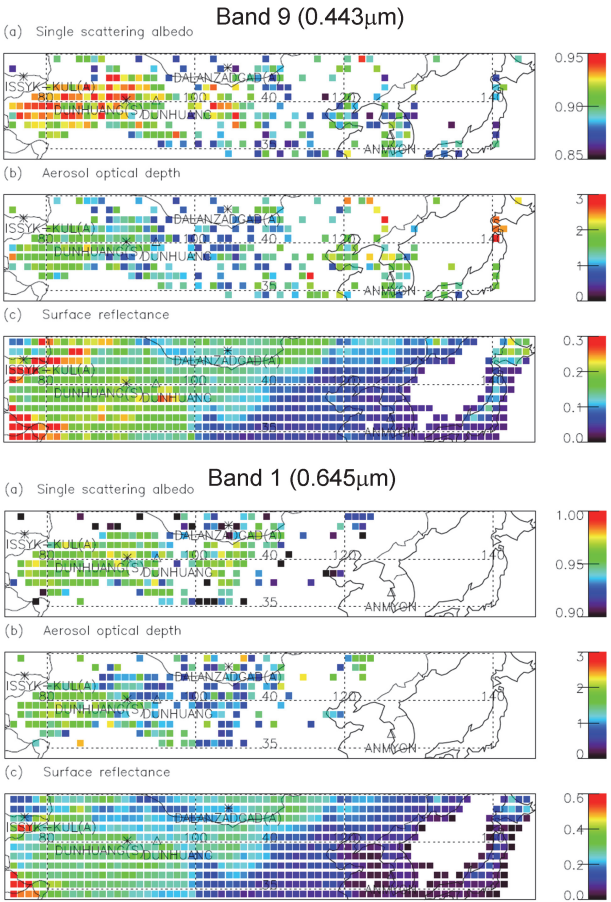

Fig. 8. This figure is identical to Fig. 7 but shows the results for Asia. The months used for the estimation are March–May because the season of dust activity is different than in the Sahara. The ground observation sites for (A) AERONET and (S) SKYNET are also shown. The triangle indicates the observation sites from Kim et al. (2004), Kim et al. (2005), and Sohn et al. (2007).

ACPD
12, 31107–31151, 2012

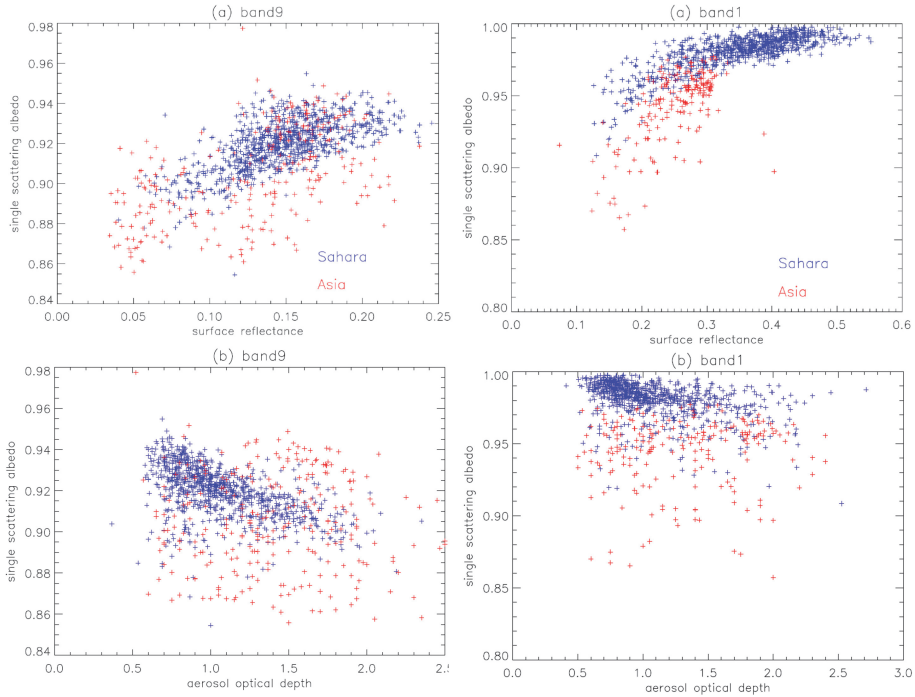

Fig. 9. Scatter plot between **(a)** the single scattering albedo ω_0 and the surface reflectance and **(b)** ω_0 and the aerosol optical depth τ_a. The red dots indicate the results in Asia and the blue dots indicate those in the Sahara. Each dot in the scatter plot corresponds to the value for 1 degree and 1 degree of resolution, as shown in Figs. 7 and 8. The MODIS data used for the analysis are the same as those in Figs. 7 and 8.

ACPD
12, 31107–31151, 2012

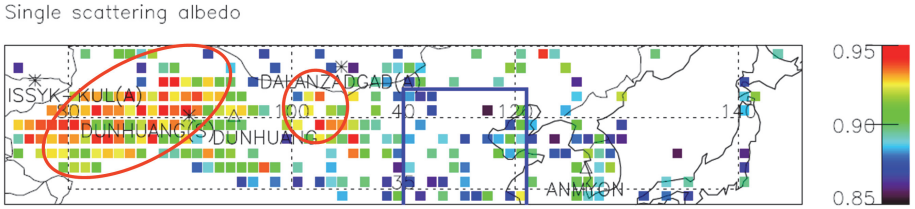

Fig. 10. This figure is identical to Fig. 8a, the spatial distribution of the single scattering albedo in band 9 over Asia, but shows the areas of typical behaviours of particular aerosols reported in the previous studies, as the red circles and blue box. The red circles correspond to the region with the large dust emissions calculated by a global aerosol transport model (Mukai et al., 2004). The blue box corresponds to the region in which coal-burning smoke mixed with dust was observed with ozone monitoring instrument observation (Herman et al., 1997).

ACPD
12, 31107–31151, 2012

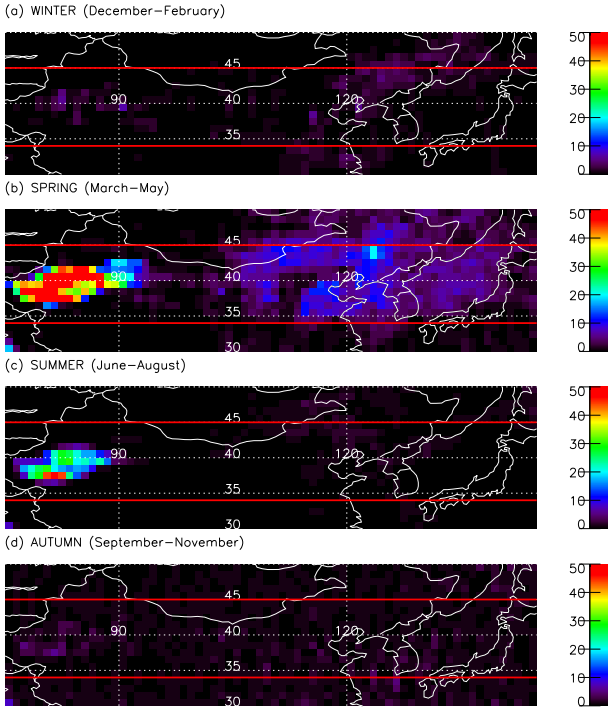

Fig. 11. Number of samples of daily data with TOMS aerosol index (AI) > 3 in **(a)** winter (December–February), **(b)** spring (March–May), **(c)** summer (June–August), and **(d)** autumn (Sebtember–November) using the data of 2005–2009. The region used for the analysis of dust optical properties in Figs. 8–10 are indicated as the red line.

ACPD
12, 31107–31151, 2012